INTERNATIONAL JOURNAL FOR NUMERICAL METHODS IN FLUIDS, VOL. 24, 355–373 (1997)

NUMERICAL UNCERTAINTIES IN TRANSONIC FLOW CALCULATIONS FOR AEROFOILS WITH BLUNT TRAILING EDGES

ROBERT D. LOTZ, BRIAN E. THOMPSON AND CHRISTOPHER A. KONINGS

Department of Mechanical Engineering, Aeronautical Engineering, and Mechanics, Rensselaer Polytechnic Institue, Troy, NY 12180–3590, U.S.A.

AND

FARHAD DAVOUDZADEH

Applied Physics Laboratory, Pensylvania State University, State College, PA, U.S.A.

SUMMARY

Numerical uncertainties are quantified for calculations of transonic flow around a divergent trailing edge (DTE) supercritical aerofoil. The Reynolds-averaged Navier–Stokes equations are solved using a linearized block implicit solution procedure and mixing-length turbulence model. This procedure has reproduced measurements around supercritical aerofoils with blunt trailing edges that have shock, boundary layer and separated regions. The present effort quantifies numerical uncertainty in these calculations using grid convergence indices which are calculated from aerodynamic coefficients, shock location, dimensions of the recirculating region in the wake of the blunt trailing edge and distributions of surface pressure coefficients. The grid convergence index is almost uniform around the aerofoil, except in the shock region and at the point where turbulence transition was fixed. The grid convergence index indicates good convergence for lift but only fair convergence for moment and drag and also confirms that drag calculations are more sensitive to numerical error.

KEY WORDS: computational fluid dynamics; transonic airfoils; numerical uncertainty

1. INTRODUCTION

Supercritical aerofoils are designed to have a roof-top pressure distribution[1] and this usually results in nearly parallel upper and lower surfaces near the trailing edges.[2] A sharp trailing edge results in a very thin structure in this highly loaded aft section of the aerofoil and so blunt trailing edges are preferred in practice, although the blunt shape causes base drag that increases overall drag in transonic cruise.[3] Henne and Gregg[4] and Henne[5] designed divergent trailing edge (DTE) aerofoils to reduce drag creep on blunt supercritical aerofoils at high subsonic Mach numbers. DTE aerofoils are designed by increasing the aerofoil thickness over the aft 10% of chord such that suction- and pressure-side flows are diverging from each other at the trailing edge. This modification to a blunt supercritical aerofoil effects an increase in the effective chord by lengthening the recirculation in the wake[6] with the result that the lift-to-drag ratio is increased, which significantly benefits aerofoil and wing aerodynamic performance.[5]

CCC 0271–2091/97/040355–19

Received 2 March 1995
Revised 29 April 1996

Calculations of transonic aerofoil flows are difficult in part because of the embedded supersonic region in an otherwise subsonic flow. This supersonic region ends in a shock wave which extends into the boundary layer on the suction side of the aerofoil and can induce flow separation on the surface.[7,8] Viscous interaction between shock and boundary layer is a complex phenomenon which has a significant influence on drag.[9] Figure 1 highlights the regions of potential problems in a transonic aerofoil calculation. Region 1 is the interaction between boundary layer and shock. Here the flow passes through a region of a strong adverse pressure gradient, which results in a thickening of the boundary layer and can lead to local separation of the flow. The displacement effect of the boundary layer reduces the effective camber in the rear of the aerofoil, and with supercritical aerofoils, which are aft loaded, the loss of lift can be up to 25% when compared with a purely inviscid calculation.[8] Region 2 is the trailing edge region. Here flow separation occurs at the sharp corners of the trailing edge and a recirculation region extends into the wake. This region has been approximately modelled by a bubble closure profile when boundary layer approximations are used, but it is preferred to calculate its dimension by solution of the Navier–Stokes equations.[10]

Computational procedures for transonic aerofoils are reviewed for example by Lock and Williams,[8] King and Williams,[11] and Cebeci *et al.*[12] and can be divided into two categories: first, viscous–inviscid interaction methods[13] which solve either integral[8] or finite difference[14] boundary layer equations near the surface and either Euler[15,16] or potential flow[17,18] inviscid equations in the freestream; second, field methods which solve the compressible Navier–Stokes equations with a turbulence model in either finite difference[19–21] or finite element[22] form.

Henne[5] calculated the transonic aerodynamics of DTE aerofoils by solving the inviscid Euler equations and integral boundary layer equations using the viscous–inviscid interaction procedure of Bauer *et al.*[2] The choice of boundary layer equations forced Henne[5] to input two approximations: first, the shape of the recirculation in the wake was provided by empirically locating the streamline that divided forward and reverse flow in the wake of the divergent trailing edge; second, an experimental correlation was used to estimate base drag, since the code[2] does not calculate any variables, including pressure, in this region. Henne[5] correlated results favourably with experiments for cruise conditions, but, since the flow immediately aft of the trailing edge had to be guessed, its influence on the observed increase in lift-to-drag ratio could not be investigated. This results in approximation of the pressure distribution and cross-flow in the rear part of the aerofoil at angles of attack higher than cruise conditions and thus the accuracy of the calculation of aerodynamic

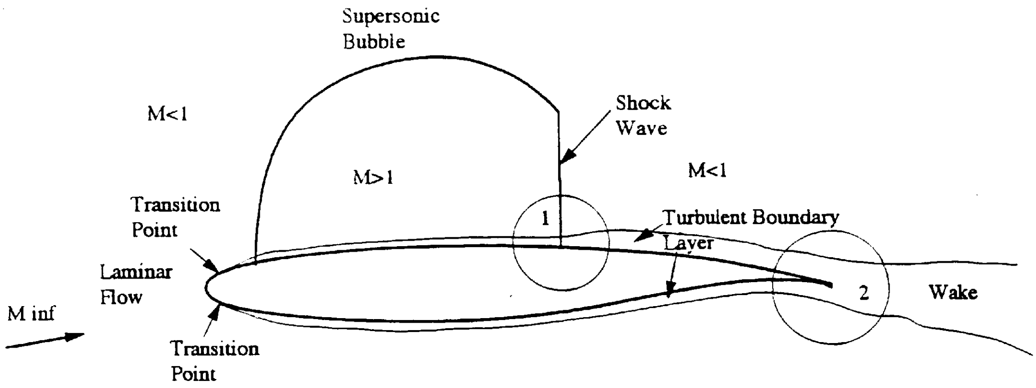

Figure 1. Sketch of flow field around supercritical aerofoil in transonic flow

coefficients is compromised.[10] In the case of the divergent trailing edge, even in cruise conditions a relatively large wake and recirculation region is present behind the trailing edge and this recirculation region has a crucial influence on the performance of the aerofoil.[14] Since boundary layer methods are unable to predict flow in the separation region, which plays a significant role in the performance of DTE aerofoils, the Navier–Stokes equations must be solved to calculate flow structures in the shock/boundary layer interaction and the recirculation region downstream of blunt divergent trailing edges on DTE aerofoils. A well-established Reynolds–averaged Navier–Stokes[19,20] calculation procedure was chosen for the present contribution for the following reasons: the entire flow field can be calculated with a single set of equations; turbulence model approximations replace profile and streamline closure assumptions; effects of the wake and normal pressure gradient, which are needed in the vicinity of recirculation, are calculated; the matching of solutions to different equations at their boundaries is eliminated. Experience suggests that computational efficiencies promised by interactive methods might not be significant when compared with the present Navier–Stokes method in this complex aerofoil flow.

The present study is a numerical assessment of the calculations by Thompson and Lotz,[14] who used a Reynolds-averaged Navier–Stokes method to compare calculations on the DLBA 186Z and DLBA 243 DTE aerofoils developed by Henne.[5] The two-dimensional, Reynolds-averaged Navier–Stokes equations in conservative form were solved using the linearized block implicit numerical procedure of Briley and McDonald,[19] which employs centred spatial differences with adjustable numerical dissipation. A mixing length turbulence model was used. Johnson and King[23] showed in calculations of a separation bubble behind a shock wave that results obtained from a simple mixing length model show good agreement with results obtained with a two-equation turbulence model. Benchmark calculations[14] with an RAE 2822 aerofoil were in good agreement with well-established experimental results. The advantages of this method are that the shape of the wake can be resolved and its effect on the performance improvement of DTE aerofoils can be investigated.

The objective of this paper is to assess the grid dependence and numerical accuracy of the aforementioned calculations. The following section describes the present choice of Navier–Stokes computational procedure including solution algorithm, grid generation, boundary conditions, turbulence model and grid dependence determination. In Section 3, solution convergence and grid convergence of global aerodynamic parameters as well as local surface pressure along the aerofoil surface are presented. Special consideration is given to the effect of the shock wave on local and global accuracy of the solution. The paper ends with summary remarks on numerical uncertainty in the present calculations and the implications for this approach when a shock is present in the flow field.

2. COMPUTATIONAL FLUID DYNAMICS METHODOLOGY

Solution algorithm

The two-dimensional, Reynolds-averaged Navier–Stokes equations were solved here in conservative form with the linearized block implicit numerical procedure of Briley and McDonald,[19,20] which employs centred spatial differences with adjustable numerical dissipation. The following equations for mass and momentum transport were solved.

Conservation of mass

$$\frac{\partial\bar{\rho}}{\partial t}+\frac{\partial}{\partial x}(\overline{\rho u_x})+\frac{\partial}{\partial y}(\overline{\rho u_y})+\frac{\partial}{\partial z}(\overline{\rho u_z})=0. \tag{1}$$

Conservation of momentum

$$\frac{\partial}{\partial t}(\overline{\rho u_x}) + \nabla \cdot (\overline{\rho u_x U}) = -\frac{\partial \bar{P}}{\partial x} + \partial \frac{\overline{\tau_{xx}}}{\partial x} + \partial \frac{\overline{\tau_{yx}}}{\partial y} + \partial \frac{\overline{\tau_{zx}}}{\partial z} + \frac{\partial}{\partial x}(-\overline{\rho u'_x u'_x}) + \frac{\partial}{\partial y}(-\overline{\rho u'_y u'_x}) + \frac{\partial}{\partial z}(-\overline{\rho u'_z u'_x}), \tag{2}$$

$$\frac{\partial}{\partial t}(\overline{\rho u_y}) + \nabla \cdot (\overline{\rho u_y U}) = -\frac{\partial \bar{P}}{\partial y} + \partial \frac{\overline{\tau_{xy}}}{\partial x} + \partial \frac{\overline{\tau_{yy}}}{\partial y} + \partial \frac{\overline{\tau_{zy}}}{\partial z} + \frac{\partial}{\partial x}(-\overline{\rho u'_y u'_x}) + \frac{\partial}{\partial y}(-\overline{\rho u'_y u'_y}) + \frac{\partial}{\partial z}(-\overline{\rho u'_z u'_y}). \tag{3}$$

Adiabatic approximation

In the present flow there is no heat addition, so the stagnation enthalpy h_0 is constant and given by

$$h_0 = \frac{T}{(\gamma - 1)M^2} + \frac{q^2}{2}, \tag{4}$$

where $q^2 = u^2 + v^2 + w^2$. With the assumption for a perfect gas that

$$P = \rho T/\gamma M^2, \tag{5}$$

the adiabatic equation of state for pressure is

$$P = \rho\left(h_0 - \frac{q^2}{2}\right)\frac{\gamma - 1}{\gamma}. \tag{6}$$

Pressure is eliminated from the momentum equations with equation (6) and temperature is evaluated from equation (5) after the flow field has been calculated. This approximation makes it unnecessary to solve the energy equation and thus reduces the computational effort required to reach a converged solution while having little effect on the calculated flow structure.

Shock treatment

Shock capturing was used to determine the location of the shock. A region with increased grid density was placed in the anticipated shock location. Shocks were recognized as regions of steep density gradients and streamwise velocity. The denser grid region was then refined to centre it on the shock until the shock location remained stable. Shock capturing smears the shock over at least one grid node, sometimes several, so shock position cannot be determined with absolute certainty.

Artificial viscosity

For high-Reynolds-number calculations it becomes necessary in the present procedure to introduce an artificial viscosity or dissipation factor into the discretized transport equations. This stabilizes the solution algorithm when boundary conditions are treated approximately, when coarse meshes are used and when there are discontinuities such as shocks in the flow. An artificial viscosity term of the form $\varepsilon_z D_z^2 \phi$, in which ε_z is given by

$$\varepsilon_z = \begin{cases} \dfrac{1}{Re}\left(\dfrac{Re_{\Delta z}}{2} - 1\right), & Re_{\Delta z} > 2, \\ 0, & Re_{\Delta z} \leqslant 2, \end{cases} \tag{7}$$

where $Re_{\Delta z}$ is the local effective mesh Reynolds number, is added to each of the discretized transport equations, with being for the continuity equation and U_x or U_y for the momentum equations. This artificial viscosity term is preceded by a constant *AVISC* which is essentially the inverse cell Reynolds number. The value of *AVISC* is selected by the user to control the amount of artificial viscosity added in various regions of the flow field and to allow its value to be reduced as the solution proceeds. In all the present calculations it was initially set equal to 0·5 for the first 400 time steps and then reduced to 0·05 following the recommendations of Davoudzadeh *et al.*[6]

Turbulence model approximations

The turbulence model used in this study was selected based on simplicity while providing reasonable accuracy. The mixing length turbulence model, although not very complex, has provided good agreement in previous work[1,14,24,25] when compared to experiments and calculations with the k–ε model, and the present calculations compare favourably with RAE 2822 experiments. In previous benchmark calculations discussed below, recirculating, transonic and aerofoil flows with the present Reynolds-averaged Navier–Stokes solution procedure were obtained, suggesting that this code calculates the lift-to-drag ratio within less than 1% for supercritical aerofoils, although absolute values of lift and drag are bounded by about 1·7% and 2·1% uncertainty respectively. The low errors obtained for L/D and drag are perhaps fortuitous, since other calculations suggest an overprediction of drag by about 5%. Measured and calculated flow structures, which includes shock and recirculating flow, are in sensible agreement and are adequate for the conclusions presented herein.

The mixing length model selected here relates the Reynolds stresses to the flow variables as

$$-\overline{\rho u_i' u_j'} = \mu_t \left[\left(\frac{\partial u_i}{\partial x_j} + \frac{\partial u_j}{\partial x_i} \right) - \frac{2}{3} \frac{\partial u_k}{\partial x_k} \delta_{ij} \right], \tag{8}$$

where μ_t is the eddy or turbulent viscosity given by

$$\mu_t = \rho l^2 \left[\left(\frac{\partial u_i}{\partial x_j} + \frac{\partial u_j}{\partial x_i} \right) \frac{\partial u_i}{\partial x_j} \right]^{1/2}. \tag{9}$$

The mixing length l is obtained from equation (10), in which y is the normal distance from the wall and D is the van Driest damping coefficient given in equation (11):

$$l = \min[l_{\max}, \kappa y D], \tag{10}$$

$$D = 1 - \exp\left(-\frac{y^+}{27} \right). \tag{11}$$

In equations (10) and (11), κ is the von Karman constant, l is determined from experiment and y^+ is the dimensionless co-ordinate normal to the wall. Their values are

$$l_{\max} = 0{\cdot}09\delta, \qquad \kappa = 0{\cdot}4, \qquad y^+ = yu_t/\nu. \tag{12}$$

The boundary layer thickness δ is the location where the local boundary layer velocity first equals 0·99 of the edge velocity. However, for the present aerofoil calculations there is no clear flow location where the edge velocity becomes independent of the distance from the wall, so the boundary layer thickness was calculated from equation (13), in which $u_{\max}$ is the maximum velocity at each streamwise location and δ is effectively twice the distance from the wall to the location where $u/u_{\max} = 0{\cdot}90$:

$$\delta = 2{\cdot}0 y_{(u/u_{\max}=c)}. \tag{13}$$

In the recirculating flow the mixing length is set with equation (14), in which h is the local height of the separated region:

$$l_{\min} = 0{\cdot}10hD. \tag{14}$$

In the wake the mixing length is proportional to the wake thickness δ calculated from equation (15), in which δ_{ps} and δ_{ss} are the thicknesses of the pressure- and suction-side boundary layers at the trailing edge respectively and X_{TE} is the trailing edge location:

$$\delta = (\delta_{\mathrm{ps}} + \delta_{\mathrm{ss}}) + 0{\cdot}2(X - X_{\mathrm{TE}}). \tag{15}$$

The present model does not calculate transition but rather fixes transition either at the location of boundary trips in wind tunnel experiments or at the suction peak where laminar separation and turbulent reattachment would be expected. Upstream of this location the laminar viscosity was calculated according to the Sutherland viscosity law:

$$\mu_\infty(T_\infty) = \frac{c_1 T_\infty^{3/2}}{c_2 + T_\infty}. \tag{16}$$

Boundary conditions

Boundary conditions are treated implicitly. At the inflow surface the total pressure is associated with the streamwise momentum equation, the cross flow velocity components are set to zero, the second derivative of the pressure is set equal to zero and the stagnation enthalpy equals the reference total enthalpy.

For the exit boundary and the upper and lower boundaries the second derivatives of the velocity components are set to zero, the pressure is defined and the second derivative of the reference total enthalpy is set to zero. At the aerofoil surface, no-slip conditions require each velocity component to be set equal to zero and the continuity equation is solved. The wall is adiabatic, with the change in enthalpy set equal to zero.

Aerodynamic force coefficients

The coefficients of lift and drag were calculated by integration of the surface pressure and skin friction over the surface of the aerofoil.

Workstation calculations

Calculations were performed on an IBM RISC 6000 Model 340 workstation with 64 MB RAM and 1 GB hard drive. Postprocessing with PLOT3D[26] produced the flow vectors, pressure contours and shock location presented below. Calculation times to reach convergence did not exceed 20 hours for the finest grid and were less than 8 hours for the coarse grid.

Benchmark calculations

The above CFD procedure needed to be validated by comparison with measurements in aerofoil flows with relevant features. The transonic flow around an RAE 2822 aerofoil exhibits boundary-layer and shock characteristics similar to those on DTE aerofoils. The 1980–81 Stanford Conference[27] assessed an RAE 2822 experiment, and based on this and subsequent recommendations, it was chosen to benchmark the CFD procedure described above. Flow structures were resolved in the very small recirculation region downstream of the blunt trailing edge and calculated aerodynamic coefficients compared well with experimental results.

Determination of grid dependence

The grid convergence index (*GCI*) proposed by Roache[28] was used to obtain a measure of the grid dependence of these calculations. The *GCI* gives a uniform measure for systematic grid refinement studies and a measure for the convergence of a discretized solution. It does not account for coding errors or insufficient iterative convergence of a code. These issues are addressed in Section 3 and prove that the solutions obtained with this code are viable and converged. The *GCI* is based on the generalized Richardson extrapolation and assumes that only ordered discretization errors exist, which would vanish if the grid spacing were reduced to zero. For a second-order method the exact solution could be represented from the solutions of a fine grid (h_1) and a coarse grid (h_2) by

$$f[\text{exact}] = \frac{h_2^2 f_1 - h_1^2 f_2}{h_2^2 - h_1^2} + \cdots . \tag{17}$$

If the method used is a second-order method with central differencing, like the method used here, f [exact] is of fourth order. Defining the refinement ratio

$$r = h_2/h_1 \tag{18}$$

and p as the order of the method, f [exact] becomes

$$f[\text{exact}] = f_1 + \frac{f_2 - f_1}{r^p - 1}. \tag{19}$$

The relative error of the fine grid is then

$$e = \frac{f_2 - f_1}{f_1} \tag{20}$$

and the fractional error is

$$E_1[\text{fine grid}] = \frac{\epsilon}{r^p - 1}. \tag{21}$$

The grid convergence index relates general grid refinement results to the results obtained from grid doubling ($r = 2$) with a second-order method ($p = 2$). The resulting definition of a grid convergence index for a comparison with a fine grid is

$$GCI[\text{fine grid}] = \frac{3|e|}{r^p - 1}, \tag{22}$$

which reduces to $GCI = |e|$ for grid doubling with a second-order method. In many cases it makes economical sense to do only one calculation with a fine grid as reference, but use the course grid for the main calculations. For this case, equation (17) is solved for the error of f_2, which results in the following *GCI* for a coarse grid solution:

$$GCI[\text{coarse grid}] = \frac{3|e|r^p}{r^p - 1} \tag{23a}$$

or

$$GCI[\text{coarse grid}] = r^p \times GCI[\text{fine grid}]. \tag{23b}$$

The Richardson extrapolation does not apply through discontinuities such as the shock encountered on the upper surface of the aerofoils used in these calculations. However, since the shock is a relatively localized discontinuity, its effect on the validity of the Richardson assumption should be small. The effect of the shock on the error estimation will be discussed in the following section. It should also be mentioned that this method allows determination of the grid dependence for arbitrary values of grid refinement. In this case the refinement ratios were 1·27 and 1·32 respectively, which represents a relatively narrow band of total refinement ratio 1·68 from coarse grid to fine grid. It is not necessary to perform a much more computationally extensive and costly doubling of the grid with this method of grid refinement.

3. RESULTS

Calculations of the flow around a DLBA 243 DTE aerofoil are presented below. The DLBA 243 DTE aerofoil is the trailing-edge-modified DLBA 186 supercritical aerofoil with a trailing edge thickness of 0·57%.[4] For this grid dependence study, calculations were performed on the coarse (140 × 95), medium (185 × 125) and fine (235 × 160) grids shown in Figures 2–4 respectively. Calculations were done at a Mach number of 0·74 at 1·809° angle of attack and a Reynolds number of $14{\cdot}5 \times 10^6$. These conditions represent the highest values of cruise Mach number and lift coefficient and result in

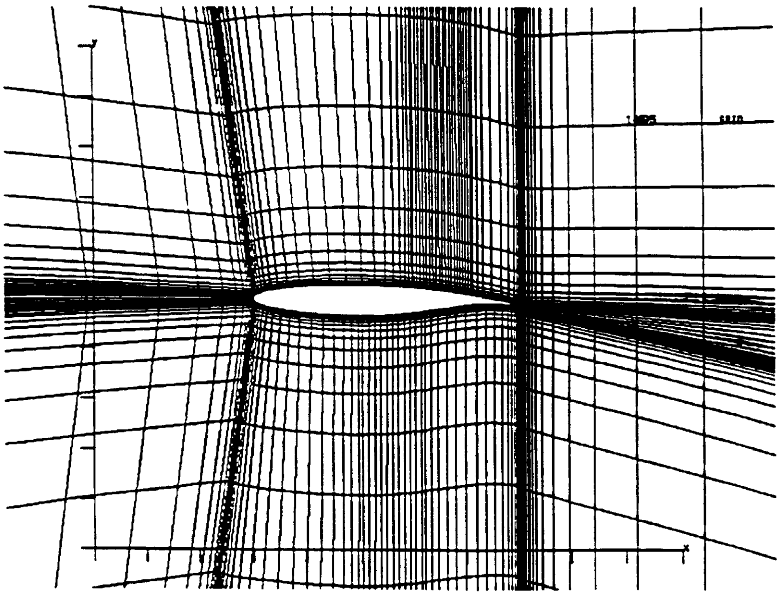

Figure 2. Coarse computational mesh for DLBA 243 aerofoil with 140 × 95 nodes

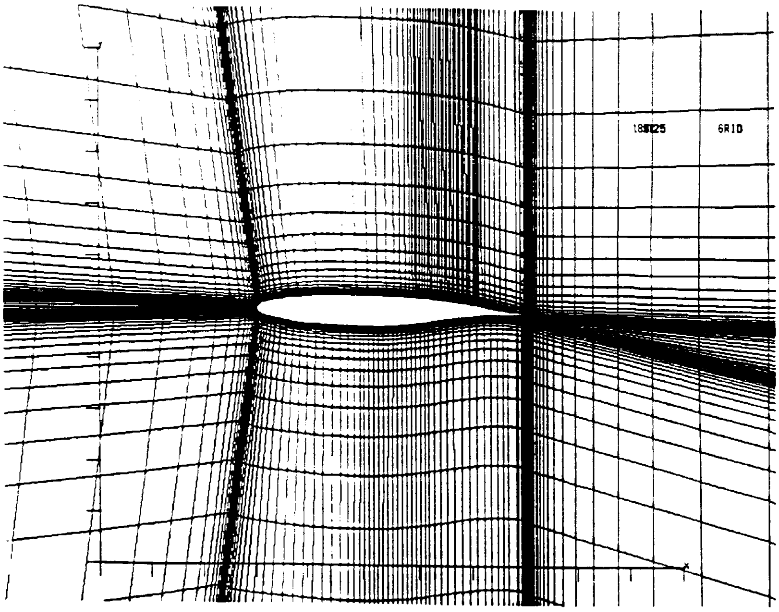

Figure 3. Medium computational mesh for DLBA 243 aerofoil with 185 × 125 nodes

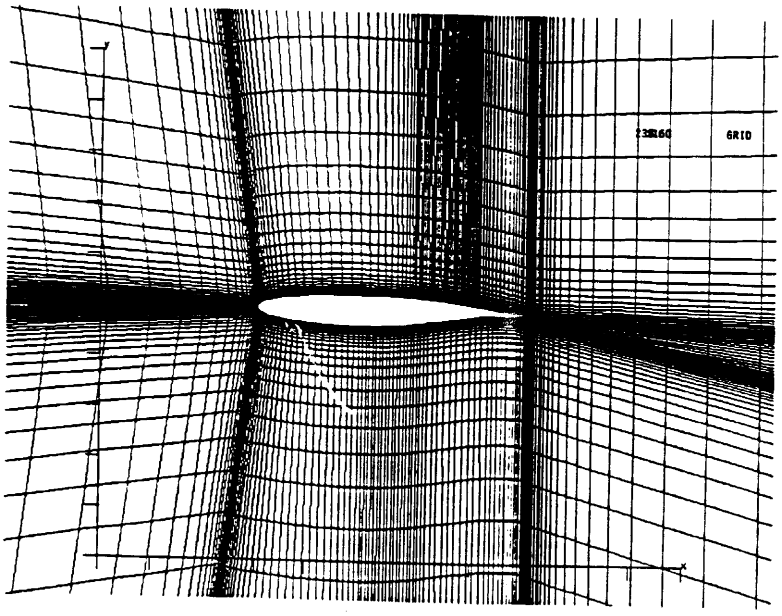

Figure 4. Fine computational mesh for DLBA 243 aerofoil with 235 × 160 nodes

the strongest shock calculated on the DTE aerofoil. Owing to the presence of a strong shock, these conditions were judged to have the largest numerical uncertainties.

Iterative convergence

The development of the aerodynamic coefficients and average residual with iterations is shown in Figures 5–8. It is apparent that after approximately 1000 iterations the slope of these curves is small, with the change in lift coefficient per time step less than 3×10^{-5}. Iterations were continued to 1400 to verify that no significant changes occur with further iterations. At 1400 iterations the slope of all aerodynamic coefficients reduces to less than 3×10^{-6} and is negligible, and lift and drag increase by only 0·30% over the values at 1000 iterations. The average residual shown in Figure 8 reduces quickly to a low value after approximately 500 iterations and then continues to decrease slowly; for practical purposes, 1000 iterations were used for production runs with the present code.[14]

Grid dependence

To assess the effect of the shock on the suction side of the aerofoil on the overall accuracy of the solution, relative differences in the surface pressure distribution are plotted along the aerofoil surface in Figure 9 and the grid convergence index in Figure 10. Agreement in the calculated surface pressure distribution of the three different grids is better than 1% to 1·3% for the fine and coarse grids respectively compared with the medium grid. Only the region of the shock has larger discrepancies of 5·5% for the fine and 40% for the coarse grid, since the shock location is shifting. Resulting lift coefficients are within 0·07% and 1·9% for the fine and coarse grids respectively compared with the medium grid. Figures 10 and 11 show the local *GCI*s on the upper and lower surfaces, respectively. The *GCI*s of the different grids is relatively uniform, increasing only slightly in the leading edge region where the transition point to turbulent flow was set, and showing a significant jump in the shock region. Upstream and downstream of the shock the *GCI* remains constant at less than 10% of

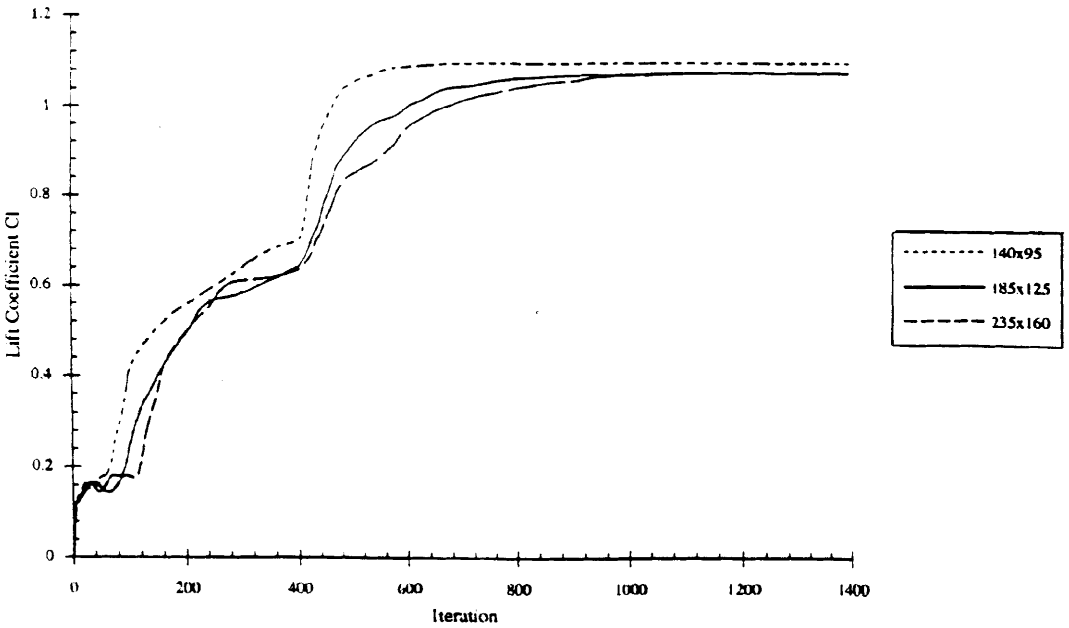

Figure 5. Time history of lift coefficient

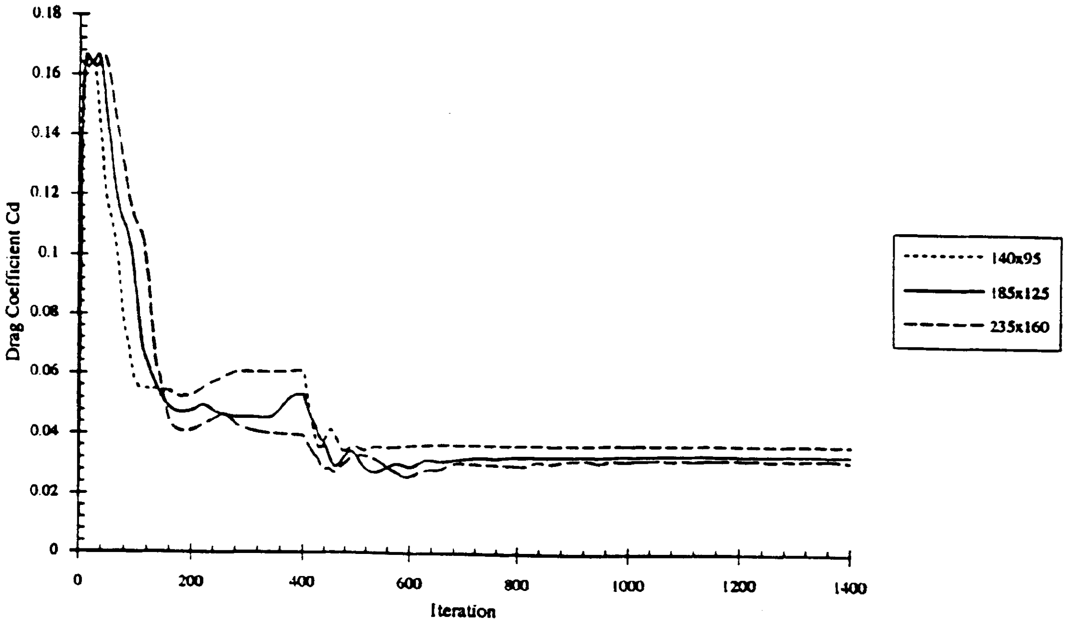

Figure 6. Time history of drag coefficient

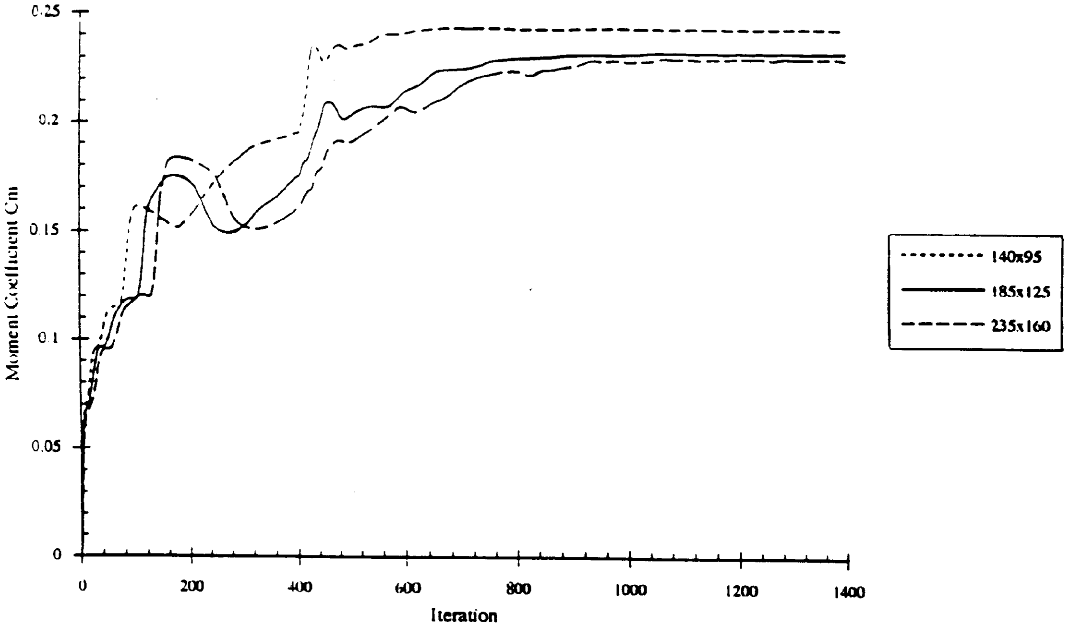

Figure 7. Time history of moment coefficient

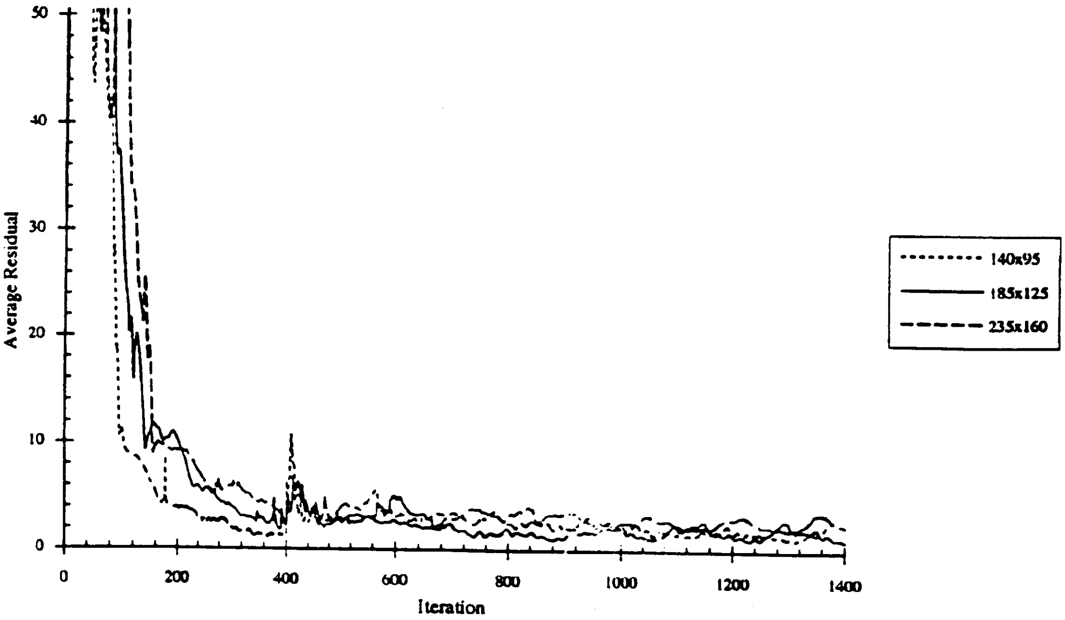

Figure 8. Time history of average residual

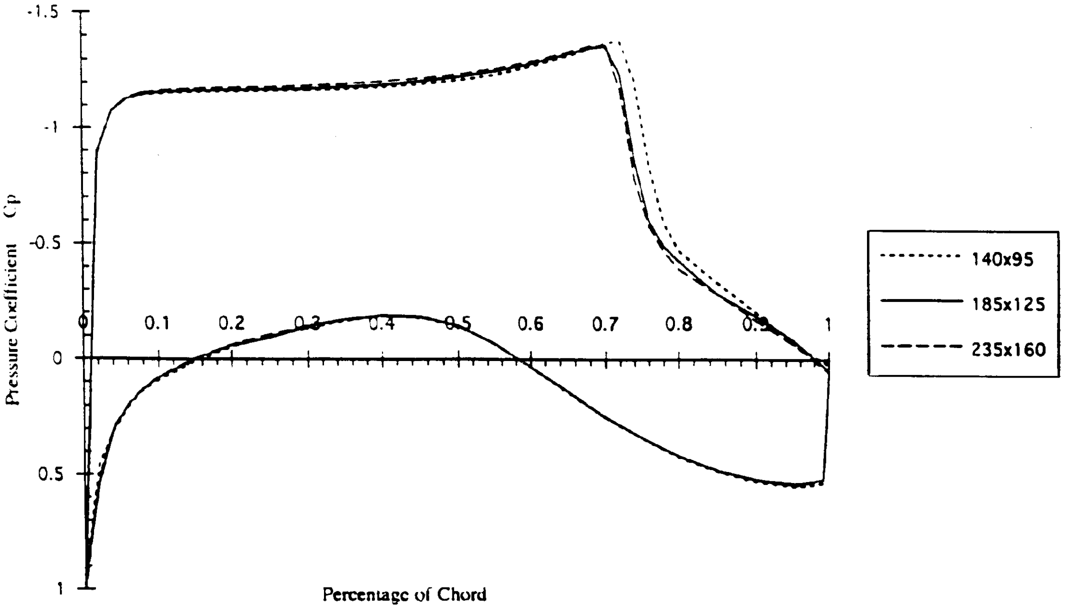

Figure 9. Calculated surface pressure distribution with coarse, medium and fine meshes

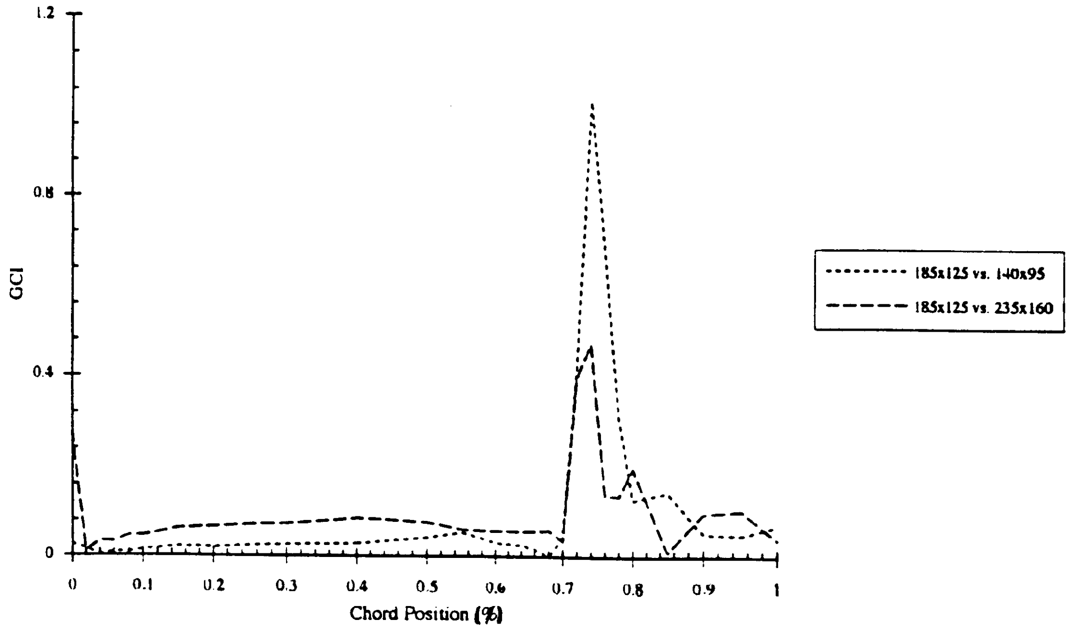

Figure 10. Grid convergence indices for pressure coefficient on suction-side surface

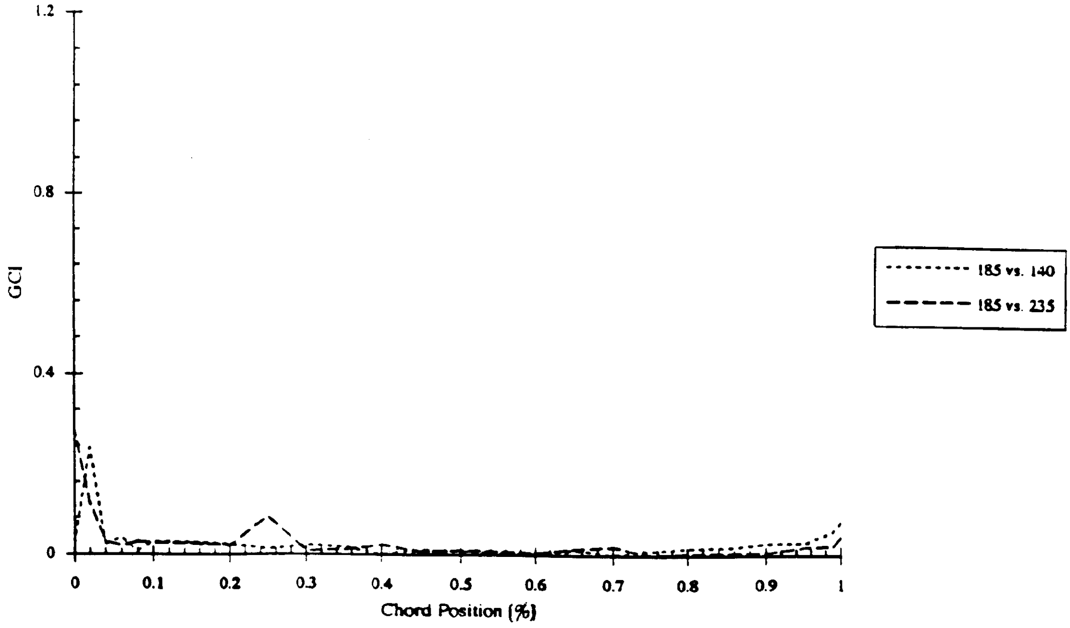

Figure 11. Grid convergence indices for pressure coefficient on the pressure-side surface

its maximum in the shock. Also, *GCI* for both the fine and coarse grid solutions are of the same order of magnitude, suggesting near-asymptotic behaviour of the solution with increasing refinement of the grid.

Resolution

Figures 12–14 present the pressure contours in the flow field around the aerofoil. Again agreement is very good, except on the coarse grid in the recovery region and the wake, where a considerable fluctuation of pressure can be observed. This results from the coarse spacing of the grid nodes in this region, which is insufficient to resolve either the boundary layer near the aerofoil or the recirculation region. This local disturbance has only a small effect on the overall accuracy of this grid. The resolution of the 185 × 125 node grid was judged to be adequate for the present purposes and was used for the calculations to compare supercritical aerofoils.[14]

Global grid convergence

The *GCI*s for the fine and coarse grid solutions are shown in Table I and Figure 15. Grid convergence indices achieved with the medium grid for the lift and moment coefficients are 0·07% and 2·3%, which are good values for engineering applications. The value achieved for the drag coefficient is comparatively high at 41% owing to the greater dependence of this parameter on numerical errors. However, as will be argued in the following section, the convergence achieved is adequate for engineering applications, especially performance comparisons of different aerofoils.

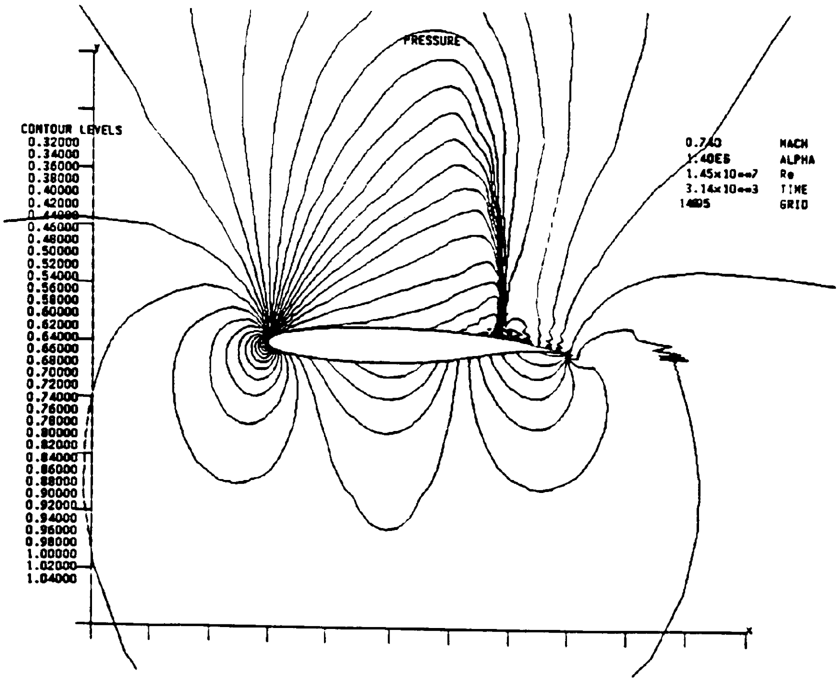

Figure 12. Distribution of pressure coefficient around DLBA 243 aerofoil calculated with the coarse mesh

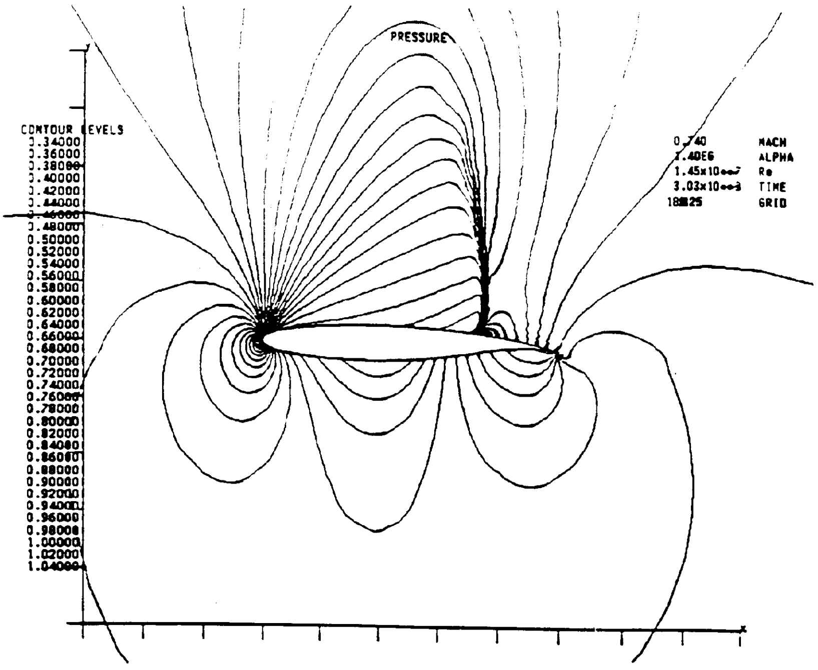

Figure 13. Distribution of pressure coefficient around DLBA 243 aerofoil calculated with the medium mesh

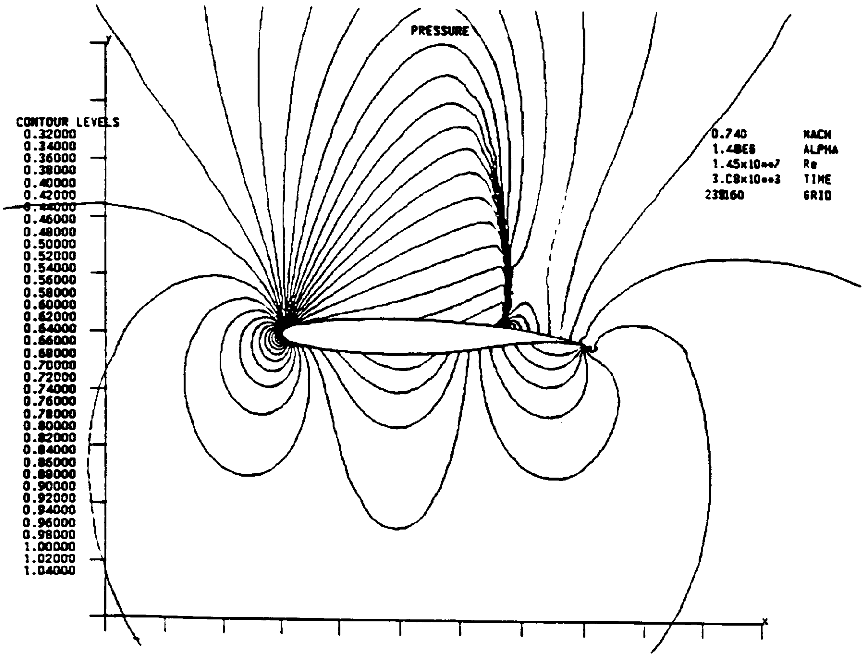

Figure 14. Distribution of pressure coefficient around DLBA 243 aerofoil calculated with the fine mesh

Table I. Grid convergence indices for DLBA 243aerofoil calculations

	Fine grid solution (140 × 95 versus 185 × 125)	Coarse grid solution (235 × 160 versus 185 × 125)
C_l	0.0772	0.0006
C_d	0·3801	0·4157
C_m	0·1852	0·0363
Shock location	0·0443	0·0880
Wake length	0·7079	0·2262
TE stagnation point	0·4634	0·2432

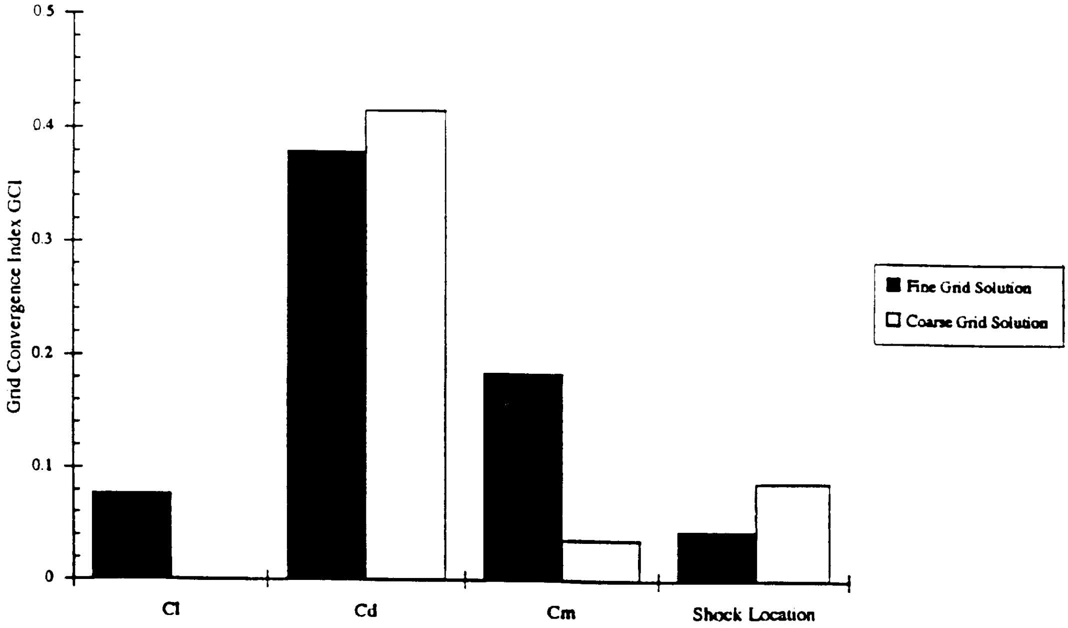

Figure 15. Grid convergence index for calculated aerodynamic coefficients and locations of flow features

Shock location varies by less than 4% between the coarse grid and the medium grid and by less than 1% between the medium grid and the fine grid, suggesting a successful use of the shock-capturing method.

4. CONCLUDING REMARKS

The main problem with calculating transonic aerofoils is accurately predicting the location and strength of the shock. The shock location is very sensitive to the properties of the grid in its vicinity and its effect on the flow field in the rear portion of the aerofoil, as well as the ultimate drag level. The shock-capturing method used here was shown to capture the shock within 1% of chord; however, it is smeared over two or three grid points and its location does not remain stationary with iterations. These oscillations of the shock propagate like pressure waves throughout the entire computational domain and act to delay convergence. Slight sinusoidal oscillations of the solution were still present after 1400 time steps, but compared with the absolute value of the solution parameter, these oscillations were less than 0·01% and negligible for engineering purposes.

Estimating the grid dependence of a transonic calculation using a simple convergence criterion such as the Richardson extrapolation, which does not take discontinuities into account, is problematic. Comparing the convergence indices between the grids, it is apparent that they give only estimates of the grid convergence index of the solution. The lift coefficient is less dependent on a realistic turbulence model, since viscous effects do not affect it very strongly. In contrast, drag is strongly dependent on smaller changes, including numerical errors, turbulence, pressure distribution and shock location, and consequently the calculated drag levels have a higher percentage uncertainty. As shown in the *GCI*s over the aerofoil, errors through the shock are large but localized. The *GCI*s calculated give an approximate determination of the reliability of the solution if the shock location is well fixed.

The grid refinement method used here allows the assessment of grid dependence with relatively small arbitrary refinement ratios. It is not necessary to perform an exact halving of the spacing resulting in a doubling of the grid size for each refinement step. In this case, the range of refinement was only 1·68 between coarse and fine grids. This illustrates the power of the *GCI* formulations, since an adequately fine grid can be determined by relatively small refinement steps, which should result in dramatic reductions in computational expense.

For the design of aerofoil sections, the main interest is in comparisons. When compared with experimental results, lift is calculated within 2% and drag within 5%, so relative lift-to-drag differences are within 7%. The calculations by Thompson and Lotz[14] clearly show that the benefits of DTE aerofoils, i.e. delayed shock, higher lift at the same angle of attack and higher L/D at the same lift coefficient of the DTE aerofoil compared with the baseline aerofoil, are resolved and magnitudes of the difference are in good agreement.

APPENDIX: NOMENCLATURE

c	chord length
c_1, c_2	experimental constants in Sutherland formula
C_d	drag/$(\frac{1}{2}\rho U^2 c)$, drag coefficient
C_l	lift/$(\frac{1}{2}\rho U^2 c)$, lift coefficient
C_m	moment/$(\frac{1}{2}\rho U^2 c^2)$, moment coefficient
D	van Driest damping coefficient
e	relative error
E	estimated fractional error
GCI	grid convergence index
h	enthalpy
h_i	grid spacing
l	characteristic length
M	Mach number
p	order of method
P	pressure
q	dynamic pressure
r	grid refinement
Re	Reynolds number
$RESAV$	average residuals
t	time

T	temperature
u, U,	velocity
x, y, z	Cartesian co-ordinates
y^+	$U_t y/$, dimensionless co-ordinate normal to wall

Greek letters

α	angle of attack
γ	specific heat ratio
δ	boundary layer thickness
ε	turbulent eddy viscosity
κ	Von Karman constant
μ	dynamic viscosity
v	kinematicviscosity
ρ	density
τ	shear stress
ϕ	transport variable

Subscripts

ps	pressure side
ss	suction side
t	time derivative
TE	conditions at trailing edge
x, y	spatial derivatives
0	stagnation conditions
1, 2	fine, coarse grid
∞	freestream conditions

REFERENCES

1. R. T. Whitcomb, ‘Review of NASA supercritical airfoils’, *Proc. Ninth Int. Cong. of the International Council of the Aeronautical Sciences (ICAS)*, 1974.
2. F. Bauer, P. Garabedian, D. Korn and A. Jameson, *Supercritical Wing Sections II*, Vol. 108, Springer, New York, 1975.
3. C. D. Harris, ‘Wind tunnel investigation of effects of trailing edge geometry on a NASA supercritical airofoil section’, *NASA TM-X-2336*, 1971.
4. P. A. Henne and R. D. Gregg, ‘New airfoil design concept’, *J. Aircraft*, 300–311 (1991).
5. P. A. Henne, ‘Innovation with computational aerodynamics: the divergent trailing-edge airfoil’, in P. A. Henne (ed.), *Applied Computational Aerodynamics*, AIAA, New York, 1990.
6. F. Davoudzadeh, R. C. Buggeln and S. J. Shamroth, *User’s Guide for the Blade Vortex Interaction Computer Code ‘BVIMINT’*, Scientific Research Associates, (prepared for NASA Ames Research Center, Contract NAS2-12635).
7. D. A. Johnson and F. W. Spaid, ‘Supercritical airfoil boundary-layer and near wake measurements’, *AIAA J.*, **20**, (1982).
8. R. C. Lock and B. R. Williams, ‘Viscous–inviscid interactions in external aerodynamics’, *Prog. Aerosp. Sci.*, **24**, 51–76 (1987).
9. R. E. Melnik, R. Chow and H. R. Mead, ‘Theory of viscous transonic flow over airfoils at high Reynolds number’, *AIAA Paper 77-680* 1977.
10. B. E. Thompson and J. H. Whitelaw, ‘Trailing-edge region of airfoils’, *J. Aircraft*, 225–234 (1989).
11. D. A. King and B. R. Williams, ‘Developments in computational methods for high-lift aerodynamics’, *Aeronaut. J.*, (1988).
12. T. Cebeci, K. Stewartson and J. H. Whitelaw, ‘Calculation of two-dimensional flow past airfoils’, in T. Cebeci (ed.), *Numerical and Physical Aspects of Aerodynamic Flows II*, Springer, New York, 1984.
13. J.-C. Le Balluer, ‘Numerical viscous–inviscid interaction in steady and unsteady flows’, in T. Cebeci (ed.), *Numerical and Physical Aspects of Aerodynamic Flows II*, Springer, New York, 1984.
14. B. E. Thompson and R. D. Lotz, ‘Divergent-trailing-edge airfoil flow’, in preparation.

15. A. W. Chen, M. M. Curtin, R. B. Carlson and E. N. Tinoco, ‘TRANAIR applications to engine/airframe integration’, *J. Aircraft*, **27**, (1990).
16. A. Jameson and D. Mavriplis, ‘Finite volume solution of the two-dimensional euler equations on a regular triangular mesh’, *AIAA J*, **24**, (1986).
17. E. N. Tinoco, D. N. Ball and F. A. Rice, ‘PAN AIR analysis of a transport high-lift configuration’, *J. Aircraft*, **24**, (1987).
18. G. Volpe and A. Jameson, ‘Transonic potential flow calculations by two artificial density methods’, *AIAA J.*, **26**, (1988).
19. W. R. Briley and H. McDonald, ‘Solution of the multi-dimensional compressible Navier–Stokes equations by a generalized implicit method’, *J. Comput. Phys.*, **24**, 372–397 (1977).
20. W. R. Briley and H. McDonald, ‘On the structure and use of linearized block implicit schemes’, *J. Comput. Phys.*, **34**, 54–73 (1980).
21. S. J. Shamroth and H. J. Gibeling, ‘Navier–Stokes solution of the turbulent flow field about an isolated airfoil’, *AIAA J.*, **18**, 1409 (1980).
22. B. E. Webster, M. S. Shephard, Z. Rusak and J. E. Flaherty, ‘Automated adaptive time-discontinuous finite element method for unsteady compressible airfoil aerodynamics’, *AIAA J.*, **32**, (1994).
23. D. A. Johnson and L. S. King, ‘A mathematically simple turbulence closure model for attached and separated turbulent boundary layers’, *AIAA J.*, **23**, (1985).
24. N.-S. Liu, F. Davoudzadeh, W. R. Briley and S. J. Shamroth, ‘Navier–Stokes simulation of transonic blade-vortex interactions’, *J. Fluids Eng.*, **112**, 501–509 (1990).
25. U. Mehta and L. Harvard, ‘Reynolds averaged Navier–Stokes computations of transonic flows—the state-of-the-art’, in D. Nixon (ed.), *Transonic Aerodynamics*, AIAA., New York, 1981.
26. P. P. Walatka, P. G. Buning, L. Pierce and P. A. Elson, ‘PLOT3D user’s manual, *NASA Tech. Memo. 101067*, 1990.
27. S. J. Kline, B. J. Cantwell and G. M. Lilley, (eds), *Proc. 1980–81 AFOSR–HTTM–Stanford Conf. on Complex Turbulent Flows: Comparison of Computation and Experiments*, Stanford, CA, September 1980.
28. P. J. Roache, ‘A method for uniform reporting of grid refinement studies’, in I. Celik, C. J. Chen, P. J. Roache and G. Scheurer (eds), *Quantification of Uncertainty in Computational Fluid Dynamics*, ASME, FED Vol. 158, New York, 1993, pp. 109–120.
29. D. Adair, B. E. Thompson and J. H. Whitelaw, ‘Measurements and calculations of a separating boundary-layer and the downstream wake’, in T. Cebeci (ed.), *Numerical and Physical Aspects of Aerodynamic Flows II*, Springer, New York, 1984.
30. D. Adair, B. E. Thompson, J. H. Whitelaw and B. R. Williams, ‘Cromparison of interactive and Navier–Stokes calculations for separated flows’, in T. Cebeci (ed.), *Numerical and Physical Aspects of Aerodynamic Flows III*, Springer, 1986.
31. T. G. Ayers, ‘Supercritical aerodynamics worthwhile over a range of speeds’, *Astronaut. Aeronaut.*, 32–36 (1972).
32. P. Bradshaw, M. A. Kavanagh and D. Mobbs, ‘Viscous–inviscid matching using imbedded Navier–Stokes solutions’, in T. Cebeci (ed.), *Numerical and Physical Aspects of Aerodynamic Flows II*, Springer, New York, 1984.
33. P. K. Chang, *Separation of Flow*, Pergamon, London, 1970.
34. F. X. Hurley, F. W. Spaid, F. W. Roos, L. S. Stivers Jr. and A. Bandettini, ‘Supercritical airfoil flowfield measurements’, *J. Aircraft*, 737–744 (1975).
35. A. M. Kuethe and C. Y. Chow, *Foundations of Aerodynamics*, Wiley, New York, 1986, pp. 276–278.
36. D. Nixon, ‘Basic equations for unsteady transonic flow’, in D. Nixon (ed.), *Unsteady Transonic Aerodynamics*, AIAA., New York, 1989.
37. P. J. Roache, ‘A method for uniform reporting of grid refinement studies’, *ASME J. Fluids Eng.*, **116**, 405–413, (1994).
38. R. L. Simpson, Y.-T. Chew and B. G. Shivaprasad, ‘The structure of a turbulent separating boundary layer’, *J. Fluid Mech.*, **113**, 23 (1981).
39. B. E. Thompson and L. Reis, ‘Comparison of finite difference calculations of a large region of recirculating flow near the trailing edge of an airfoil’, *AGARD CP 412*, 1986.
40. B. E. Thompson and J. H. Whitelaw, ‘A turbulent boundary layer approaching separation’, *Walz-Festschrift Volume*, Springer, New York, 1983, pp. 253–262.
41. B. E. Thompson and J. H. Whitelaw, ‘Characteristics of a trailing-edge flow with turbulent boundary-layer separation’, *J. Fluid Mech.*, **157**, 305–326 (1985).
42. J. F. Wendt, (ed.), *Computational Fluid Dynamics, an Introduction*, Springer, New York, 1992.